Research Article

Journal of Environmental Nanotechnology

# Green-synthesized MgO Nanoparticles Using *Cardiospermum halicacabum* for Antibacterial Activity and Hydroxylamine-assisted Reactive Orange 16 Removal

A. Lourdu Caroline[1], S. Ishwarya[2*], E. Janaki[3], P. Manivel Pandian[4], R. Venkatesh[5] and Muthezhilan Radhakrishnan[6]

[1]Department of Computer Applications, St. Joseph's College of Arts and Science (Autonomous), Cuddalore, TN, India
[2]Department of Electrical and Electronics Engineering, M. Kumarasamy College of Engineering, Karur, TN, India
[3]Department of Mathematics, Panimalar Engineering College, Poonamallee, Thiruvallur, TN, India
[4]Department of Computer Science and Engineering, NPR College of Engineering and Technology, Natham, Dindigul, TN, India
[5]Department of Mechanical Engineering, Vinayaka Mission's Kirupananda Variyar Engineering College, Vinayaka Mission's Research Foundation (Deemed to Be University) Salem, TN, India
[6]Department of Marine Biotechnology, Academy of Maritime Education and Training (AMET), Deemed to be University, Kanathur, Chennai, TN, India

Received: 28.07.2026 Accepted: 29.08.2026 Published: xx.xx.xxxx

*ishwarya.s23@gmail.com



## ABSTRACT

This study aimed to develop multifunctional magnesium oxide nanoparticles (MgO NPs) through a sustainable synthesis route using Cardiospermum*m* halicacabum leaf extract and to evaluate their antibacterial and wastewater-treatment potential. The effects of magnesium nitrate concentration, extract concentration, reaction temperature, and reaction time on MgO yield were optimized using a Taguchi L27 design and ANOVA. The novelty lies in integrating Taguchi optimization with comparative artificial neural network (ANN) and support vector regression (SVR) modelling to optimize and predict plant-mediated MgO production. The optimized nanoparticles were characterized using UV–visible spectroscopy, FTIR, XRD, and SEM–EDX and evaluated for antibacterial activity and hydroxylamine-enhanced Reactive Orange 16 removal. Extract concentration was the dominant synthesis parameter, contributing 54.02% to yield variation. The optimum conditions of 0.10 M precursor, 100 g $L^{-1}$ extract, 65 °C, and 75 min produced 0.13913 ± 0.00035 g of MgO, with only 0.09% deviation from the Taguchi prediction. The ANN and SVR models achieved cross-validated $R^2$ values of 0.9828 and 0.9999, respectively, confirming the superior predictive performance of SVR. Characterization verified the formation of crystalline cubic-periclase MgO. The nanoparticles exhibited concentration-dependent antibacterial activity. The MgO/NaClO/hydroxylamine system achieved 96.8% Reactive Orange 16 removal within 30 min, with an apparent rate constant of 0.117 $min^{-1}$. These findings demonstrate the practical potential of green-synthesized MgO nanoparticles for rapid treatment of dye-bearing wastewater. Further studies should investigate catalyst recyclability, degradation-product toxicity, mineralization efficiency, reaction mechanisms, and performance in actual textile effluents.

**Keywords:** Green synthesis; Sustainability; Optimization; ANN; Reactive orange 16.

## 1. INTRODUCTION

The continuous discharge of synthetic dyes from textile, printing, leather, and chemical industries has become one of the major environmental concerns because of high stability, toxicity, and resistance to conventional wastewater treatment methods. Among azo dyes, Reactive Orange 16 (RO16) is widely used due to its excellent dyeing properties; however, its complex aromatic structure and azo bonds make it highly persistent in aquatic environments, posing significant ecological and human health risks. Development of sustainable, highly efficient, and environmentally benign technologies for RO16 removal has attracted considerable research interest.

Adsorption is an effective approach for dye removal because of its simplicity, low energy requirement, and high efficiency. Various bio-based adsorbents have demonstrated promising RO16 removal capacities, including cross-linked chitosan-genipin/$SiO_2$ (57.1 mg $g^{-1}$), CTS-BADGE/NS (97.8 mg $g^{-1}$), and CS-EPH/NSi bionanocomposites (110.2 mg $g^{-1}$), while selenium-doped mesoporous biochar achieved 538 mg $g^{-1}$ through π–π interactions, pore filling, and hydrogen bonding (Wu *et al.* 2024a); (Abdulhameed *et al.* 2024); (Wu *et al.* 2024b); (Dos Reis *et al.* 2023). However, adsorption primarily transfers dye molecules from the aqueous phase to the adsorbent, highlighting the need for complementary advanced oxidation and photocatalytic processes for effective degradation.

Semiconductor nanoparticles have emerged as promising photocatalysts for persistent organic pollutants because of their high surface area, catalytic activity, and reactive oxygen species generation. Ce-substituted Mn–Zn ferrite nanoparticles achieved 97.25% Congo Red and 98.42% RO16 degradation under visible light within 120 min, while green-synthesized CuO nanoparticles and oyster shell-derived nHAp/$TiO_2$/GO nanocomposites achieved 96.37% Congo Red and nearly 98% methylene blue degradation, respectively (Dinesh *et al.* 2022); (Boddu *et al.* 2025); (Vanitha *et al.* 2023). These findings demonstrate the potential of metal oxide nanomaterials for sustainable wastewater remediation

Among semiconductor oxides, ZnO nanoparticles have attracted considerable attention because of their wide band gap, high electron mobility, chemical stability, low toxicity, and low cost. Plant-mediated synthesis further improves their environmental compatibility by using phytochemicals as natural reducing, stabilizing, and capping agents. Garcinia cambogia-mediated ZnO nanoparticles demonstrated efficient degradation of cationic and anionic dyes with antibacterial activity, while Prosopis glandulosa-derived ZnO achieved 95.24% methylene blue removal with an adsorption capacity of 88.5 mg $g^{-1}$ (Sasi *et al.* 2022). These studies highlight the potential of green-synthesized ZnO nanomaterials for integrated adsorption and photocatalytic applications.

In addition to catalytic degradation, multifunctional nanomaterials possessing antimicrobial properties have become increasingly attractive for integrated environmental remediation. Organo-montmorillonite/silver nanocomposites simultaneously achieved complete antibacterial inhibition against Escherichia coli and Staphylococcus aureus while effectively removing textile dyes (Sadeghianmaryan *et al.* 2022). Fungus-mediated Ag–Fe bimetallic nanoparticles exhibited efficient methylene blue removal together with strong antibacterial activity and enhanced seed germination, demonstrating multifunctional environmental applications (Patel *et al.* 2025). Furthermore, green-synthesized silver nanoparticles have shown remarkable anticancer activity by inducing apoptosis and suppressing cell proliferation (Kotteeswaran *et al.* 2024), highlighting the broad biomedical potential of biologically synthesized nanomaterials.

Recent advances have also demonstrated the importance of integrating artificial intelligence (AI) with nanomaterial synthesis and environmental applications. Machine learning algorithms have significantly improved process optimization, prediction accuracy, and experimental efficiency. XGBoost coupled with a genetic algorithm successfully optimized Nano-ZnO synthesis, producing nanoparticles with high yield, large specific surface area, and crystallite sizes below 20 nm while achieving a prediction accuracy of $R^2 = 0.956$ (Guo *et al.* 2026). Artificial neural networks (ANNs) have accurately predicted Cu(II) adsorption using nano zero-valent aluminum, outperforming conventional regression models with extremely low prediction errors (Sadek *et al.* 2023). Similarly, ANN, support vector regression (SVR), and random forest models successfully optimized membrane performance for water treatment applications (Mohammad *et al.* 2025). These findings indicate that machine learning has become a valuable tool for optimizing synthesis parameters and predicting nanoparticle performance.

However, limited studies have combined plant-mediated MgO nanoparticle synthesis with statistical optimization and machine-learning-assisted modelling for enhanced catalytic removal of Reactive Orange 16. The novelty of this study lies in integrating the *Cardiospermum halicacabum*-mediated green synthesis of magnesium oxide nanoparticles with Taguchi L27–ANOVA optimization and comparative ANN–SVR modelling. Unlike conventional synthesis approaches, the proposed method uses plant-derived phytochemicals as natural complexing and stabilizing agents, thereby reducing the need for hazardous chemicals. The optimized MgO nanoparticles were further applied in hydroxylamine-enhanced catalytic oxidation of Reactive Orange 16, establishing a sustainable and multifunctional approach that combines data-driven nanoparticle production with rapid treatment of dye-contaminated wastewater.

## 2. MATERIALS AND METHODOLOGY

### 2.1 Materials and Reagents

Fresh *Cardiospermum halicacabum* leaves were obtained from Anthiyur, Erode, Tamil Nadu during April and May 2026. Magnesium nitrate hexahydrate [$Mg(NO_3)_2 \cdot 6H_2O$] was employed as the magnesium precursor, while Reactive Orange 16 served as the target dye. Sodium hydroxide (NaOH), Hydroxylamine hydrochloride ($NH_2OH \cdot HCl$), ethanol, hydrochloric acid (HCl), and other necessary analytical-grade reagents were purchased from Star Scientific Enterprises, Erode, Tamil Nadu, India. All substances were utilized directly without further purification. Distilled water was used for preparing the leaf extract, precursor solution, and dye samples. Before each experiment, the glassware was thoroughly cleaned with dilute hydrochloric acid, repeatedly rinsed using distilled water and completely dried.

### 2.2 Preparation of *Cardiospermum halicacabum* Leaf Extract

The *Cardiospermum halicacabum* leaves was collected from Anthiyur, Tamil Nadu, India, between April and May 2026. The samples were repeatedly rinsed

with distilled water to remove dust and surface impurities and shade-dried at ambient temperature for ten days. Dried leaves were converted into fine powder using a GM300 Retsch electric grinder. For aqueous extraction, 10.0 g of leaf powder was mixed with 100 mL of DI water and heated at 85 °C for 10 min with continuous magnetic stirring (Kavitha *et al.* 2021). After cooling, the mixture was centrifuged at 10,000 rpm. The supernatant was vacuum-filtered through Whatman No. 1 filter paper. The prepared extract was stored at 4 °C until further use.

## 2.3 Green Synthesis of Magnesium Oxide Nanoparticles

Magnesium oxide nanoparticles were prepared using *Cardiospermum halicacabum* leaf extract as a natural complexing and stabilizing medium. A 0.1 M magnesium nitrate solution was produced by dissolving 2.56 g of $Mg(NO_3)_2{\cdot}6H_2O$ in 100 mL of DIW. The prepared leaf extract was introduced dropwise into the precursor solution under constant magnetic stirring at 700 rpm and 62 °C for 1 h (Sahith *et al.* 2025). Sodium hydroxide solution was added to promote magnesium hydroxide precipitation. The development of a whitish suspension indicated particle formation. Phytochemicals present in the extract facilitated nucleation, restricted particle growth, and stabilized the resulting structures. The proposed transformations are:

Dissociation of magnesium nitrate hexahydrate:

$$Mg(NO_3)_2 \cdot 6H_2O \rightarrow Mg^{2+} + 2NO_3 + 6H_2O \quad \ldots (1)$$

Formation of magnesium hydroxide:

$$Mg^{2+} + 2OH^- \rightarrow Mg(OH)_2 \quad \ldots (2)$$

Thermal conversion into magnesium oxide:

$$Mg(OH)_2 \xrightarrow{\Delta} MgO + H_2O \quad \ldots (3)$$

The precipitate was separated by centrifugation and washed using distilled water and ethanol. It was subsequently vacuum-filtered through a 0.22 µm membrane and dried at 60 °C for 12 h (Amale *et al.* 2026). The dried material was calcined at 500 °C for 3 h to obtain MgO NPs. Finally, the prepared nanoparticles were stored in a light-protected container at room temperature until analysis.

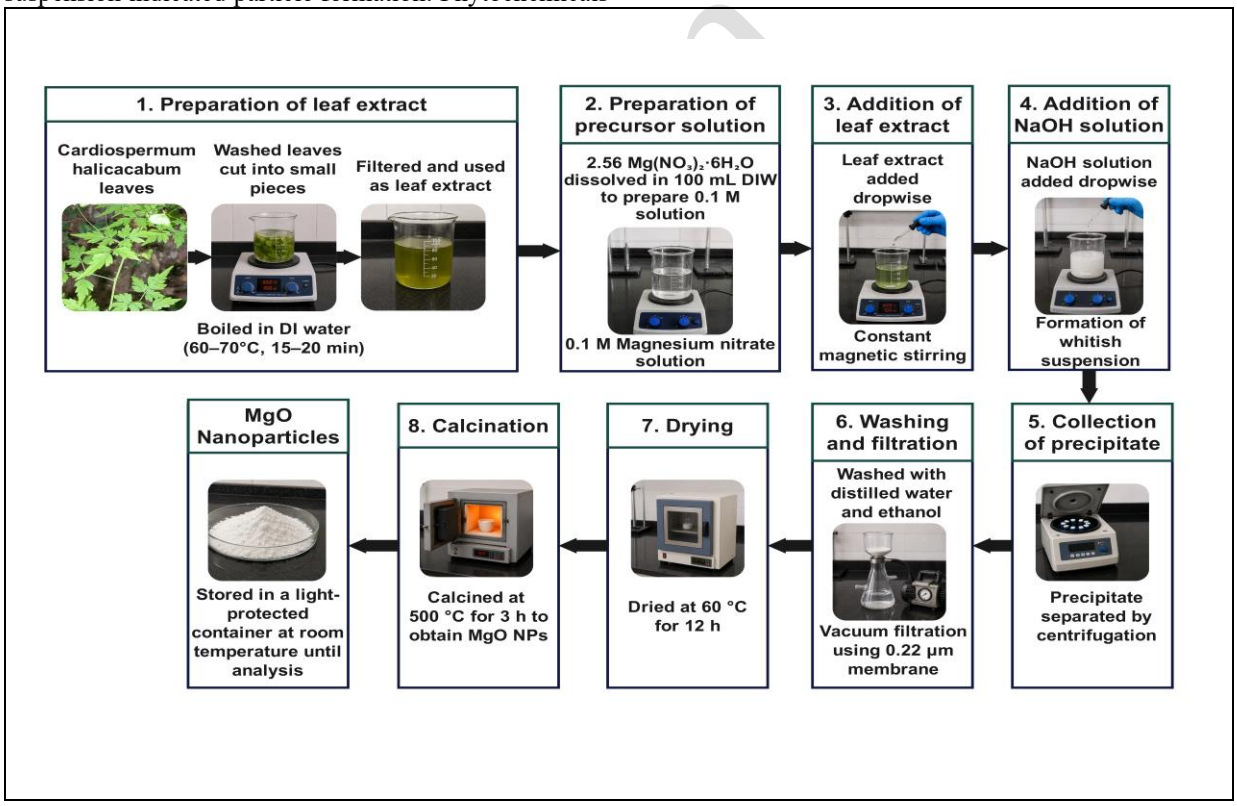


**Fig. 1: Green synthesis pathway of MgO nanoparticles**

## 2.4 Taguchi L27 Optimization on the Synthesis of MgO Nanoparticles

A Taguchi L27 orthogonal array was constructed in Minitab to maximize the yield of magnesium oxide nanoparticles (MgO NPs) produced using *Cardiospermum halicacabum* leaf extract. The resulting design comprised 27 experimental combinations. The investigated variables were $Mg(NO_3)_2{\cdot}6H_2O$ concentration (A), leaf-extract

concentration (B), reaction temperature (C), and reaction duration (D). The selected factors and levels are presented in Table 1.

**Table 1. Factors and levels used in the Taguchi L27 design**

| Code | Synthesis Factor | Unit | Level 1 | Level 2 | Level 3 |
|---|---|---|---|---|---|
| A | $Mg(NO_3)_2 \cdot 6H_2O$ concentration | M | 0.05 | 0.10 | 0.15 |
| B | *C. halicacabum* extract concentration | g $L^{-1}$ | 50 | 100 | 150 |
| C | Reaction temperature | °C | 50 | 65 | 80 |
| D | Reaction time | min | 45 | 60 | 75 |

The combination of these factor and levels generated 27 experimental runs. The recovered dry mass of MgO nanoparticles after washing, drying, and calcination was selected as the response (Y). The complete experimental matrix and corresponding yield values are presented in Table 2.

**Table 2. Taguchi L27 experimental matrix and MgO nanoparticle dry yield**

| Run | $Mg(NO_3)_2 \cdot 6H_2O$ (M) | Extract (g $L^{-1}$) | Temperature (°C) | Time (min) | MgO dry yield (g) |
|---|---|---|---|---|---|
| 1 | 0.05 | 50 | 50 | 45 | 0.0748 |
| 2 | 0.1 | 50 | 50 | 45 | 0.0873 |
| 3 | 0.15 | 50 | 50 | 45 | 0.0809 |
| 4 | 0.05 | 100 | 65 | 60 | 0.1196 |
| 5 | 0.1 | 100 | 65 | 60 | 0.1324 |
| 6 | 0.15 | 100 | 65 | 60 | 0.1258 |
| 7 | 0.05 | 150 | 80 | 75 | 0.1087 |
| 8 | 0.1 | 150 | 80 | 75 | 0.1212 |
| 9 | 0.15 | 150 | 80 | 75 | 0.1149 |
| 10 | 0.05 | 50 | 65 | 75 | 0.1018 |
| 11 | 0.1 | 50 | 65 | 75 | 0.1145 |
| 12 | 0.15 | 50 | 65 | 75 | 0.1077 |
| 13 | 0.05 | 100 | 80 | 45 | 0.1039 |
| 14 | 0.1 | 100 | 80 | 45 | 0.1162 |
| 15 | 0.15 | 100 | 80 | 45 | 0.1098 |
| 16 | 0.05 | 150 | 50 | 60 | 0.0976 |
| 17 | 0.1 | 150 | 50 | 60 | 0.1104 |
| 18 | 0.15 | 150 | 50 | 60 | 0.1038 |
| 19 | 0.05 | 50 | 80 | 60 | 0.0869 |
| 20 | 0.1 | 50 | 80 | 60 | 0.0995 |
| 21 | 0.15 | 50 | 80 | 60 | 0.0931 |
| 22 | 0.05 | 100 | 50 | 75 | 0.1146 |
| 23 | 0.1 | 100 | 50 | 75 | 0.1275 |
| 24 | 0.15 | 100 | 50 | 75 | 0.1207 |
| 25 | 0.05 | 150 | 65 | 45 | 0.1015 |
| 26 | 0.1 | 150 | 65 | 45 | 0.1141 |
| 27 | 0.15 | 150 | 65 | 45 | 0.1079 |

Analysis of variance was applied to determine the statistical contribution and significance of all synthesis parameters. Signal-to-noise ratio was calculated by the "larger-is-better" criterion because nanoparticle yield was intended to be maximized (Chowdhury *et al.* 2026):

$$S/N = -10\log_{10}\left[\frac{1}{n}\sum_{i=1}^{n}\frac{1}{Y_i^2}\right] \quad \ldots (4)$$

Main-effect plots, factor rankings, percentage contributions, and interaction trends were examined to identify the parameter combination producing the highest MgO NP yield.

## 2.5 Confirmation Tests

The optimum factor levels obtained from the Taguchi analysis were verified experimentally. MgO NPs were synthesized under the predicted operating conditions, and their measured dry yield was compared with the estimated response. Model reliability was assessed from the percentage deviation between the predicted and experimental results:

$$\text{Deviation}(\%) = \frac{|Y_{\text{exp}} - Y_{\text{pred}}|}{Y_{\text{exp}}} \times 100 \quad \ldots (5)$$

A low deviation indicated satisfactory agreement and confirmed the suitability of the optimized synthesis conditions.

## 2.6 ANN and SVR Modeling

Artificial neural network (ANN) and support vector regression (SVR) models were developed to describe the nonlinear relationship between the four synthesis variables and MgO NP yield.

Before model development, the variables were normalized between 0 and 1 using:

$$x_i = \frac{X - X_{\text{min}}}{X_{\text{max}} - X_{\text{min}}} \quad \ldots (6)$$

where $x_i$ shows the normalized value, $X$ is the original observation, and $X_{\text{min}}$ and $X_{\text{max}}$ represent its minimum and maximum limits. The ANN architecture was selected by varying the number of hidden neurons and choosing the configuration with minimum prediction error and maximum determination coefficient.

The ANN employed a feed-forward multilayer perceptron consisting of four input neurons, a hidden layer, and one output neuron (Alanazi *et al.* 2025). During forward propagation, the weighted input values were transferred through the hidden layer and transformed using an activation function to generate the predicted MgO nanoparticle yield. The prediction error was determined from the difference between the experimental and predicted yields. During backpropagation, the network weights and biases were iteratively adjusted to minimize this prediction error. The ANN architecture was selected by varying the number of hidden neurons and choosing the configuration with the minimum prediction error and maximum coefficient of determination.

The same experimental inputs and responses were used to construct the SVR model. SVR maps the input variables into a higher-dimensional feature space and constructs a regression function within an ε-insensitive error margin. A kernel function was employed to represent the nonlinear relationships between the synthesis parameters and MgO nanoparticle yield. Only observations outside the ε-insensitive region, known as support vectors, contributed directly to the final regression function. The regularization parameter C, kernel parameter, and ε value were tuned through cross-validation to balance prediction accuracy and model generalization.

Cross-validation was employed for both ANN and SVR models to reduce dependence on a single training–testing division and assess their ability to predict unseen observations. ANN and SVR accuracy was compared using mean squared error (MSE) and the coefficient of determination (R2) (Lateef *et al.* 2022):

$$\text{MSE} = \frac{1}{n}\sum_{i=1}^{n} \left(Y_{i,\text{exp}} - Y_{i,\text{pred}}\right)^2 \quad \ldots (7)$$

$$R^2 = 1 - \frac{\sum_{i=1}^{n} \left(Y_{i,\text{exp}} - Y_{i,\text{pred}}\right)^2}{\sum_{i=1}^{n} \left(Y_{i,\text{exp}} - \bar{Y}_{\text{exp}}\right)^2} \quad \ldots (8)$$

The model exhibiting the lowest MSE and highest $R^2$ was considered more reliable for predicting MgO nanoparticle yield.

## 2.7 Characterization of Green-synthesized MgO Nanoparticles

### 2.7.1 Optical Analysis by UV–visible Spectroscopy

The absorption properties of prepared magnesium oxide nanoparticles were examined using UV–visible spectroscopy (Dhanaraj *et al.* 2024). The resulting spectrum was also employed to estimate their optical bandgap. Measurements were recorded from 200 to 600 nm with a Thermo Scientific EVOLUTION 260 BIO spectrophotometer. Quartz cuvettes were used for sample analysis, and distilled water served as the blank reference.

### 2.7.2 Fourier-transform Infrared Spectral Analysis

The chemical bonds and surface functional groups associated with *Cardiospermum halicacabum* leaf extract and the green-synthesized magnesium oxide nanoparticles were evaluated before and after calcination at 500 °C for 3 h. FTIR spectra were acquired using a Shimadzu IRAffinity-1S instrument over a wavenumber range of 4000–500 $cm^{-1}$.

### 2.7.3 Crystalline Structure Analysis by X-ray Diffraction

The phase purity, crystal structure, and average crystallite size of green-synthesized magnesium oxide nanoparticles were determined by X-ray diffraction. Patterns were recorded by a Philips X'Pert diffractometer

with Cu Kα radiation (λ = 1.5406 Å) and operated at 20 mA (Prajudtasri *et al.* 2025). Diffraction intensities were collected across a 2θ interval of 20–80° to verify MgO crystallinity and detect any secondary crystalline phases.

#### 2.7.4 Morphological and Elemental Examination by SEM–EDX

Surface morphology, shape, particle dimensions, and elemental distribution of purified magnesium oxide nanoparticles were investigated by scanning electron microscopy coupled with EDX. SEM micrographs were obtained at scale bars of 2 µm, 1 µm, and 500 nm.

### 2.8 Antimicrobial Performance of Green-synthesized MgO Nanoparticles

#### 2.8.1 Microorganisms

The antimicrobial potential of magnesium oxide nanoparticles prepared using *Cardiospermum halicacabum* leaf extract was investigated against selected bacterial strains. The bacterial panel included Gram-positive species *Staphylococcus aureus* ATCC 25923and *Bacillus subtilis* ATCC 6633, together with the *Escherichia coli* ATCC 25922 and Gram-negative species *Pseudomonas aeruginosa* ATCC 27853 (Karthick *et al.* 2026).

#### 2.8.2 Disc-diffusion Assessment of Antibacterial Activity

Antibacterial performance of magnesium oxide nanoparticles synthesized using *Cardiospermum halicacabum* leaf extract was evaluated against four bacterial strains using the Kirby–Bauer disc-diffusion method (Huang *et al.* 2023). Each bacterial suspension was adjusted to the 0.5 McFarland standard, corresponding to approximately $1.5 \times 10^8$ CFU $mL^{-1}$. Mueller–Hinton agar plates containing 20 mL of medium were uniformly inoculated with the respective bacterial cultures. Sterile 5 mm filter-paper discs were loaded with MgO nanoparticle suspensions at concentrations of 0.05, 0.25, 0.50, 1.00, 2.00, 5.00, and 10.00 mg $mL^{-1}$ and placed on the inoculated agar. The prepared plates were maintained at 4 °C for 30 min and subsequently incubated at 36 °C for 24 h. Antibacterial effectiveness was quantified by measuring the diameter of the inhibition zone surrounding each disc. All experiments were performed in triplicate (n = 3), and inhibition-zone diameters were expressed as mean ± standard deviation. Statistical differences among MgO nanoparticle concentrations were evaluated using one-way analysis of variance (ANOVA), followed by Tukey's post-hoc multiple-comparison test. Differences were considered statistically significant at $p < 0.05$.

### 2.9 Catalytic Degradation of Reactive Orange 16 Using MgO Nanoparticles

Reactive Orange 16 removal was investigated using green-synthesized magnesium oxide nanoparticles in the presence and absence of hydroxylamine (Hussain *et al.* 2026). A 20 mg $L^{-1}$ dye solution was transferred into a 250 mL beaker and agitated in the dark for 30 min to establish equilibrium. Subsequently, 5 mg of MgO nanoparticles were introduced. Separate experiments were performed using $H_2O_2$ and NaClO as oxidizing agents, both with and without 2 M hydroxylamine hydrochloride. The reaction pH was maintained at the experimentally selected value (Rao *et al.* 2025). Aliquots of 2 mL were withdrawn, and residual dye absorbance was measured at the maximum absorption wavelength of Reactive Orange 16, approximately 493 nm. Dye-removal efficiency was calculated using eqn (9) (Kaur and Pal, 2026):

$$R(\%) = \frac{C_0 - C_t}{C_0} \times 100 = \frac{A_0 - A_t}{A_0} \times 100 \quad \ldots (9)$$

## 3. RESULTS AND DISCUSSION

### 3.1 Green Formation of MgO Nanoparticles

Magnesium oxide nanoparticles were produced through a sustainable route using Cardiospermum halicacabum leaf extract as a natural complexing and stabilizing medium. Gradual introduction of the extract into the $Mg(NO_3)_2 \cdot 6H_2O$ solution, followed by alkaline precipitation, changed the initially transparent mixture into a whitish suspension, indicating magnesium hydroxide formation (Fig. 2). Phytochemicals in the extract supported nucleation and restricted excessive particle aggregation by interacting with magnesium ions. Subsequent drying and calcination at 500 °C converted the precipitated $Mg(OH)_2$ into crystalline MgO nanoparticles. The final white powder confirmed successful thermal transformation, while further verification was obtained from UV–visible, FTIR, XRD, and SEM–EDX analyses.

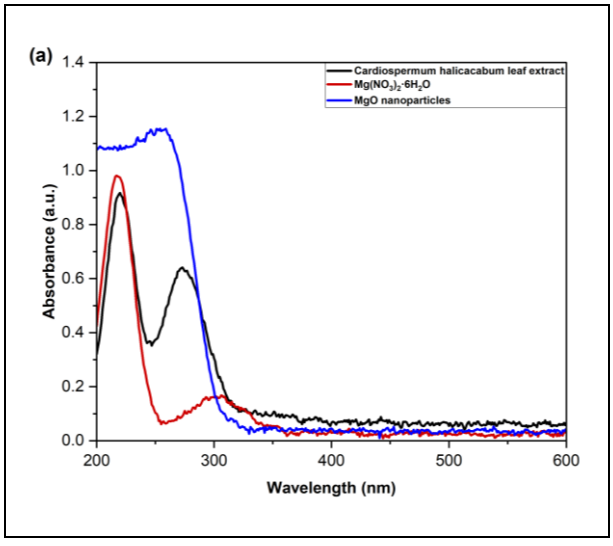

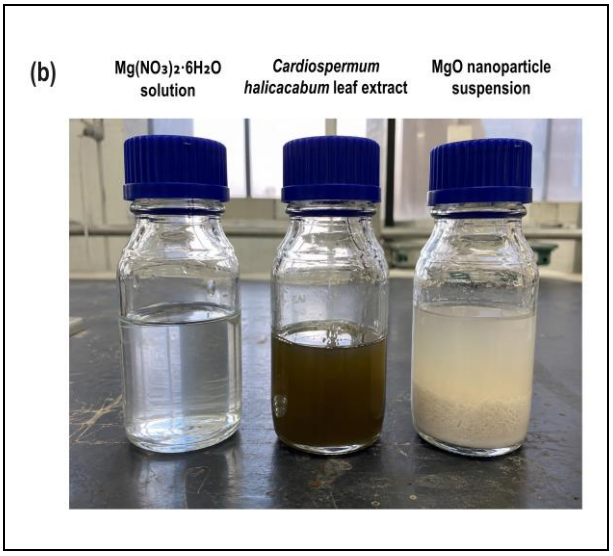


**Fig. 2: UV–visible characterization of green-synthesized MgONPs: (a) spectra of MgONPs, $Mg(NO_3)_2 \cdot 6H_2O$, and *Cardiospermum halicacabum* leaf extract and (b) visual confirmation of MgONP biosynthesis**

## 3.2 Taguchi L27 Analysis and ANOVA

The dry yield MgO nanoparticle varied from 0.0748 to 0.1324 g across the Taguchi L27 experiments. The highest observed yield of 0.1324 g was obtained at 0.10 M $Mg(NO_3)_2 \cdot 6H_2O$, 100 g $L^{-1}$ extract, 65 °C, and 60 min.

**Table 3. Response table for the mean of dry yield MgO nanoparticle at different factor levels**

| Level | $Mg(NO_3)_2 \cdot 6H_2O$ Concentration (M) | Extract Concentration (g $L^{-1}$) | Reaction Temperature (°C) | Reaction Time (min) |
|---|---|---|---|---|
| 1 | 0.10104 | 0.09406 | 0.10196 | 0.09960 |
| 2 | 0.11368 | 0.11894 | 0.11392 | 0.10768 |
| 3 | 0.10718 | 0.10890 | 0.10602 | 0.11462 |
| Delta | 0.01263 | 0.02489 | 0.01197 | 0.01502 |
| Rank | 3 | 1 | 4 | 2 |

The response table for means (Table 3) indicated that, extract concentration had the largest effect, followed by reaction time, precursor concentration, and temperature. The highest mean responses were obtained at A2, B2, C2, and D3.

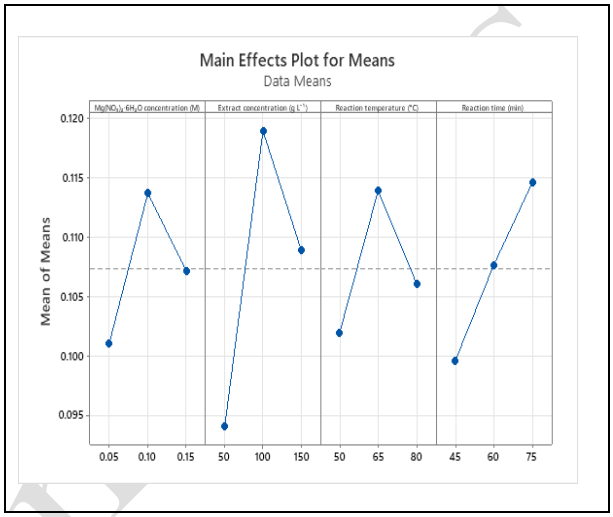


**Fig. 3: Main-effect plot for the mean of dry yield MgO nanoparticle obtained from the Taguchi L27 design**

The main-effects plot for means (Figure 3) showed that yield increased when precursor concentration, extract concentration, and temperature were raised from Level 1 to Level 2, but decreased at Level 3. Reaction time produced a progressive increase in yield from 45 to 75 min.

**Table 4. Response table for signal-to-noise ratios of MgO nanoparticle yield**

| Level | $Mg(NO_3)_2 \cdot 6H_2O$ Concentration (M) | Extract Concentration (g $L^{-1}$) | Reaction Temperature (°C) | Reaction Time (min) |
|---|---|---|---|---|
| 1 | -19.99 | -20.61 | -19.96 | -20.13 |
| 2 | -18.95 | -18.52 | -18.90 | -19.44 |
| 3 | -19.47 | -19.28 | -19.54 | -18.83 |
| Delta | 1.04 | 2.09 | 1.06 | 1.30 |
| Rank | 4 | 1 | 3 | 2 |

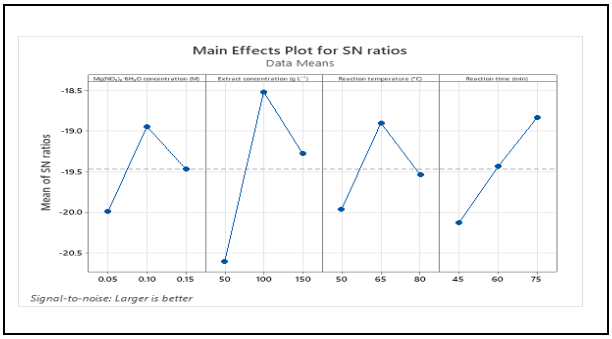


**Fig. 4: Main-effect plot for S/N of MgO nanoparticle dry yield**

The S/N-ratio response table (Table 4) ranked extract concentration as the most influential factor, followed by reaction time, temperature, and precursor concentration. The largest S/N ratios occurred at A2B2C2D3.

As shown in Figure 4, the optimum synthesis condition was 0.10 M $Mg(NO_3)_2 \cdot 6H_2O$, 100 g $L^{-1}$ extract, 65 °C, and 75 min. The corresponding Taguchi-predicted yield was 0.13926 g

.

**Table 5. ANOVA results for the Taguchi L27 optimization of MgO nanoparticle dry yield**

| Source | DF | Sequential SS | Contribution (%) | Adjusted SS | Adjusted MS | F-value | p-value |
|---|---|---|---|---|---|---|---|
| $Mg(NO_3)_2 \cdot 6H_2O$ concentration (M) | 2 | 0.000718 | 13.75 | 0.000718 | 0.000359 | 22,909.82 | <0.001 |
| Extract concentration (g $L^{-1}$) | 2 | 0.002822 | 54.02 | 0.002822 | 0.001411 | 89,996.60 | <0.001 |
| Reaction temperature (°C) | 2 | 0.000666 | 12.76 | 0.000666 | 0.000333 | 21,252.83 | <0.001 |
| Reaction time (min) | 2 | 0.001017 | 19.47 | 0.001017 | 0.000509 | 32,445.57 | <0.001 |
| Residual error | 18 | <0.000001 | 0.01 | <0.000001 | <0.000001 | — | — |
| Total | 26 | 0.005225 | 100.00 | — | — | — | |

ANOVA results (Table 5) confirmed that all four synthesis factors were statistically significant ($p<0.001$). Extract concentration exhibited the highest contribution of 54.02%, followed by reaction time at 19.47%, precursor concentration at 13.75%, and temperature at 12.76%. Therefore, extract concentration was the dominant parameter controlling MgO nanoparticle production.

## 3.3 Confirmation Tests

A confirmation experiment was conducted at the Taguchi-optimized condition of 0.10 M $Mg(NO_3)_2 \cdot 6H_2O$, 100 g $L^{-1}$ *C. halicacabum* extract, 65 °C, and 75 min. The three confirmation runs produced MgO yields of 0.1388, 0.1395, and 0.1391 g, respectively. The mean experimental yield was 0.13913±0.00035 g, which was close to the Taguchi-predicted value of 0.13926 g. The deviation between the predicted and experimental yields was only 0.09%, confirming the reliability of the Taguchi optimization.

## 3.4 ANN and SVR Prediction

ANN and SVR models were constructed to predict MgO nanoparticle yield from precursor concentration, extract concentration, reaction temperature, and reaction duration (Ahmad *et al.* 2023). The ANN and SVR models produced cross-validated $R^2$ values of 0.9828 and 0.9999, respectively, demonstrating excellent predictive performance. The prediction errors were further evaluated using RMSE and MAE. The ANN model produced RMSE and MAE values of 0.00182 and 0.00155 g, respectively, whereas the SVR model achieved substantially lower values of 0.00014 and 0.00011 g, respectively. These lower error values confirm the closer agreement of the SVR predictions with the experimental MgO nanoparticle yields and demonstrate its superior predictive accuracy.

**Table 6. Confirmation of the Taguchi-optimized MgO nanoparticle synthesis condition**

| Result | Value |
|---|---|
| Optimum condition | 0.10 M, 100 g $L^{-1}$, 65 °C and 75 min |
| Taguchi-predicted yield | 0.13926 g |
| Confirmation run 1 | 0.1388 g |
| Confirmation run 2 | 0.1395 g |
| Confirmation run 3 | 0.1391 g |
| Mean confirmation yield | (0.13913±0.00035) g |
| Prediction deviation | 0.09% |

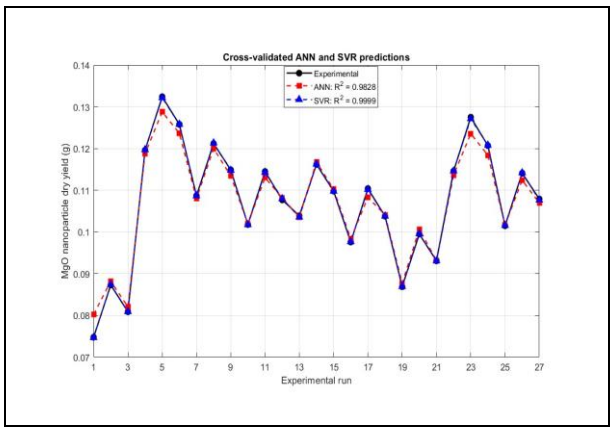


**Fig. 5: Experimental and cross-validated ANN and SVR predicted MgO nanoparticle yields for Taguchi L27 runs**

Both models closely followed the experimental yield pattern. However, the SVR predictions showed closer agreement with the observed values than the ANN predictions.

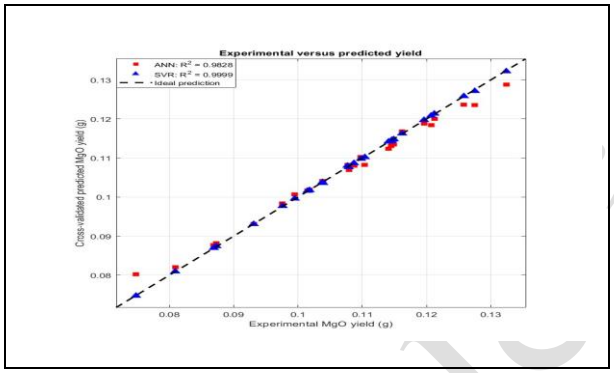


**Fig. 6: Experimental versus cross-validated ANN and SVR predicted MgO nanoparticle yields**

The SVR points were positioned close to the ideal prediction line, confirming its superior prediction accuracy. At the optimum condition, ANN and SVR predicted yields of 0.13385 and 0.13919 g, respectively. The SVR result differed from the Taguchi prediction by only 0.05%.

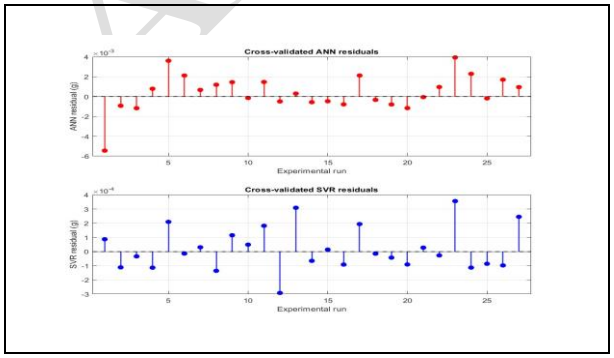


**Fig. 7: Cross-validated residual distributions of the ANN and SVR models for MgO nanoparticle-yield prediction**

The SVR residuals were smaller and more closely distributed around zero than the ANN residuals. Therefore, SVR was selected as the more reliable model for predicting MgO nanoparticle yield.

## 3.5 Characterization of MgO Nanoparticles

### 3.5.1 UV–visible Absorption Analysis

Optical responses of *Cardiospermum halicacabum* leaf extract and optimized magnesium oxide nanoparticles were examined between 200 and 600 nm. The plant extract displayed absorption bands near 220 and 273 nm, which can be associated with electronic transitions of phenolic and other phytochemical constituents. These compounds may assist magnesium-ion complexation, particle nucleation, and surface stabilization during green synthesis. The MgO nanoparticle spectrum exhibited a characteristic absorption edge around 305 nm, supporting the formation of nanoscale magnesium oxide. Changes in absorption intensity and band position between the extract and MgO sample further indicated the participation of plant-derived functional groups in nanoparticle development. Minor displacement of the MgO absorption edge may arise from variations in crystallite dimensions, morphology, surface defects, agglomeration, and preparation conditions. The MgO nanoparticle spectrum exhibited a characteristic absorption edge around 305 nm, supporting the formation of nanoscale MgO. A similar absorption peak at 294 nm and an optical band gap of 4.52 eV were reported for green-synthesized MgO nanoparticles, indicating that the observed optical response is consistent with previously reported MgO nanostructures (Kiran *et al.* 2023).

### 3.5.2 FTIR Investigation of Surface Functional Groups

FTIR spectra of *Cardiospermum halicacabum* leaf extract and magnesium oxide nanoparticles before and after calcination were recorded between 4000 and 500 $cm^{-1}$. This analysis identified the biomolecular groups involved in magnesium-ion complexation, nanoparticle nucleation, and surface stabilization. As illustrated in Fig. 8, leaf extract showed broad band near 3294 $cm^{-1}$, assigned to O–H stretching in phenolic and alcohols compounds. The signal at approximately 2925 $cm^{-1}$ originated from aliphatic C–H stretching. Absorption around 1602 $cm^{-1}$ was associated with carbonyl stretching and aromatic vibrations of plant-derived constituents. The bands near 1384 and 1050 $cm^{-1}$ corresponded to C–N and C–O stretching, respectively. Several of these organic signals remained in the uncalcined nanoparticles, confirming phytochemical attachment to their surfaces. After calcination at 500 °C, their intensities decreased substantially because of organic-material decomposition. Meanwhile, a prominent absorption region between approximately 615

and 548 $cm^{-1}$ appeared, corresponding to Mg–O lattice vibrations and supporting MgO nanoparticle formation.

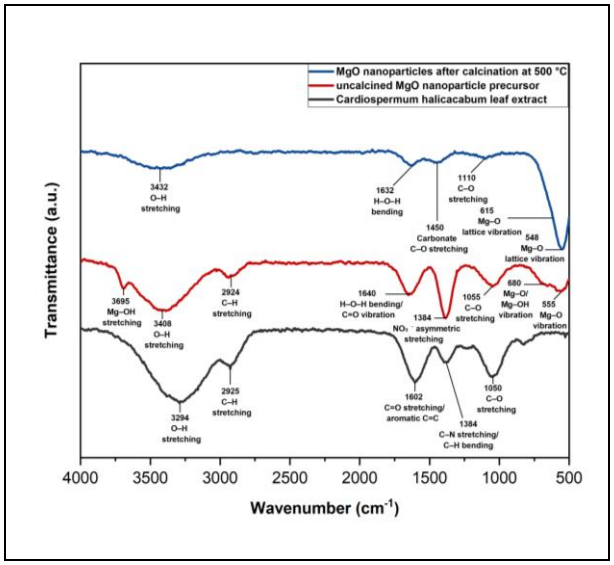


**Fig. 8: FTIR spectra of *Cardiospermum halicacabum* leaf extract, uncalcined MgO nanoparticle precursor, and MgO nanoparticles after calcination at 500 °C**

The formation of magnesium oxide nanoparticles was supported by characteristic absorption bands appearing within 500–620 $cm^{-1}$, particularly near 548 and 615 $cm^{-1}$, which were assigned to Mg–O lattice vibrations. These signals became more prominent after calcination, confirming the conversion of the magnesium hydroxide precursor into MgO. Compared with the plant-extract spectrum, the uncalcined nanoparticle sample showed shifted bands near 3408, 1640, 1384, and 1055 $cm^{1}$. These spectral changes indicate that biomolecules in the leaf extract participated in magnesium-ion complexation, nucleation, and particle stabilization. Most organic absorption bands weakened or disappeared following calcination because the attached plant-derived compounds underwent thermal decomposition. These Mg–O vibrational bands are comparable to the 541–552 $cm^{-1}$ region reported for green-synthesized MgO nanoparticles from plant peel extracts, further confirming successful conversion of the precursor into crystalline MgO (Badilli *et al.* 2026).

**Table 7. FTIR peak assignments of leaf extract and MgO nanoparticles**

| Sample | Peak ($cm^{-1}$) | Assignment | Interpretation |
|---|---|---|---|
| Leaf extract | 3294 | O–H stretching | Phenolic and alcoholic compounds |
| Leaf extract | 2925 | Aliphatic C–H stretching | Plant-derived organic constituents |
| Leaf extract | 1602 | C=O stretching/aromatic vibrations | Carbonyl-containing phytochemicals |
| Leaf extract | 1384 | C–N stretching | Nitrogen-containing biomolecules |
| Leaf extract | 1050 | C–O stretching | Alcohols, phenols and polysaccharides |
| Uncalcined MgO precursor | 3408 | O–H stretching | Surface hydroxyl groups and attached phytochemicals |
| Uncalcined MgO precursor | 1640 | C=O/aromatic vibrations | Phytochemical interaction with $Mg^{2+}$ ions |
| Uncalcined MgO precursor | 1384 | C–N stretching | Residual plant-derived compounds |
| Uncalcined MgO precursor | 1055 | C–O stretching | Surface-bound organic constituents |
| Calcined MgO NPs | 615 and 548 | Mg–O lattice vibrations | Formation of crystalline MgO |

The principal FTIR absorption bands and their corresponding functional-group assignments are summarized in Table 7. The shifts observed in the uncalcined precursor indicate phytochemical involvement in $Mg^{2+}$ complexation and particle stabilization, whereas the prominent Mg–O bands after calcination confirm MgO formation.

#### 3.5.3 Crystalline-phase Evaluation by X-ray Diffraction

XRD analysis were conducted to verify the structure and crystalline phase of the green-synthesized magnesium oxide nanoparticles and to estimate their average crystallite size. Figure 8 presents the pattern of MgO nanoparticles prepared by *Cardiospermum halicacabum* leaf extract. Distinct reflections observed at approximately 36.91°, 42.88°, 62.27°, 74.64°, and 78.58° corresponded to the (111), (200), (220), (311), and (222) crystallographic planes, respectively. These reflections confirmed the formation of the face-centred cubic periclase structure of MgO and agreed with the ICDD reference pattern PDF 45-0946, which displayed corresponding reflections at 36.94°, 42.92°, 62.30°, 74.69°, and 78.63°. The absence of prominent secondary-phase reflections indicated the effective conversion of the precursor into crystalline MgO during calcination. No intense peaks associated with residual $Mg(OH)_2$ or $Mg(NO_3)_2 \cdot 6H_2O$ were detected, indicating

successful precursor conversion and satisfactory phase purity after calcination. These reflections closely match those reported at 36.94°, 42.86°, 62.30°, 74.70°, and 78.62° for green-synthesized MgO nanoparticles, confirming the same phase-pure cubic periclase structure (Muhaymin *et al.* 2024).

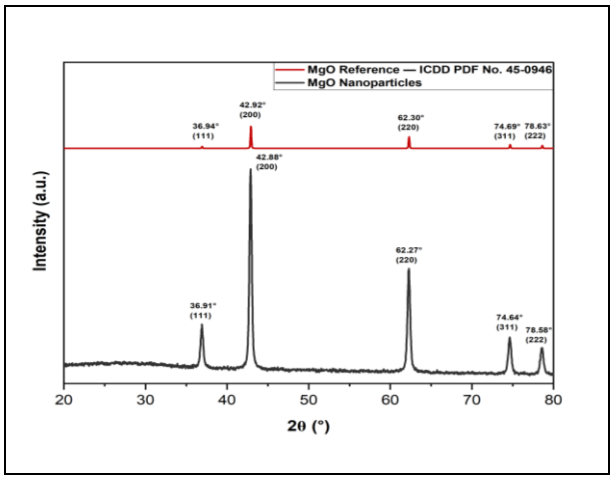


**Fig. 9: X-ray diffraction pattern of green-synthesized MgO nanoparticles after calcination at 500 °C**

**3.5.4 Morphological and Elemental Assessment by SEM–EDX**

The elemental composition and morphology of magnesium oxide nanoparticles prepared by aqueous *Cardiospermum halicacabum* leaf extract were examined by SEM–EDX. Micrographs obtained at different magnifications revealed predominantly irregular, granular, and quasi-spherical particles with approximate primary-particle dimensions (Fig. 10). Considerable agglomeration was observed, which was attributed to the high surface energy, van der Waals interactions, and surface hydroxyl groups of the MgO nanoparticles. Precursor concentration, extract dosage, reaction temperature, pH, and phytochemical composition may influence nucleation, particle growth, morphology, and aggregation.

EDX spectroscopy and elemental mapping confirmed magnesium and oxygen as the principal constituents of the prepared nanoparticles. Their measured weight percentages were 57.6% Mg and 39.1% O, supporting MgO formation. A weak carbon signal of 3.3% was also recorded and may originate from residual plant-derived compounds or the carbon adhesive used during sample preparation. No substantial impurity signals were detected, indicating satisfactory elemental purity. These values closely match the 57.25% Mg and 38.99% O reported for green-synthesized MgO nanoparticles by (Seghir *et al.* 2023), further confirming the elemental purity of the prepared nanoparticles.

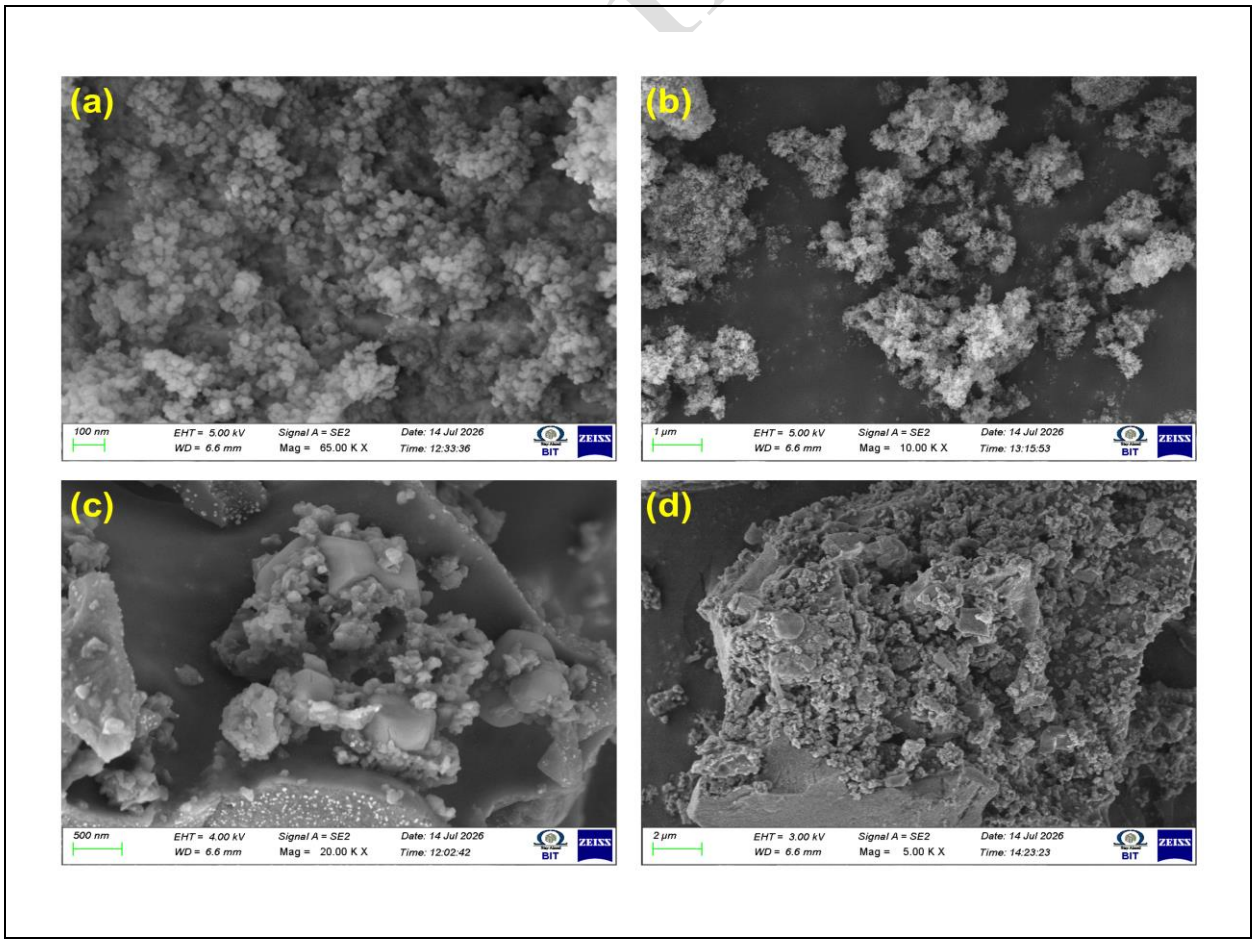

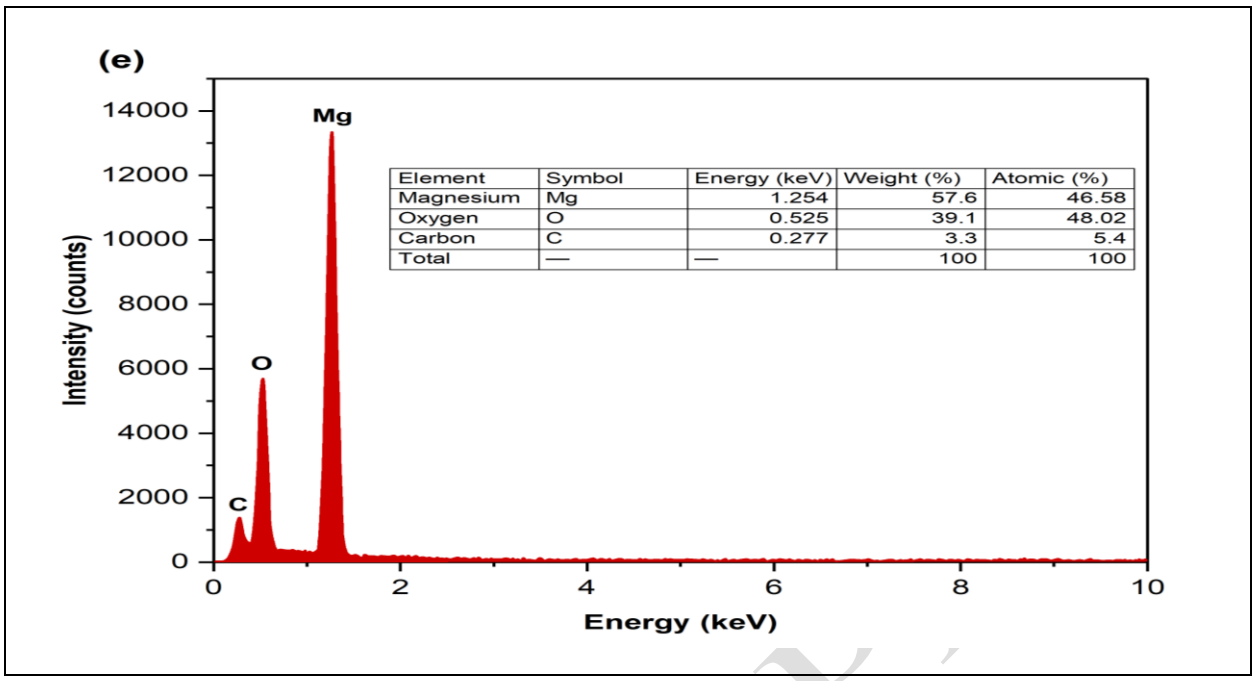


**Fig. 10: (a-e) SEM micrographs, and EDX spectrum of MgO nanoparticles synthesized using *Cardiospermum halicacabum* leaf extract**

The SEM images revealed predominantly irregular, granular, and quasi-spherical MgO nanoparticles with considerable agglomeration. Extensive particle overlap prevented reliable determination of individual particle sizes and particle-size distribution. EDX confirmed Mg and O as the major elements, supporting successful MgO formation and satisfactory elemental purity.

## 3.6 Antimicrobial Performance

### 3.6.1 Antibacterial Response

Antibacterial activity of the green-synthesized magnesium oxide nanoparticles was evaluated against the Gram-positive bacteria *Bacillus subtilis* and *Staphylococcus aureus* and the Gram-negative bacteria *Escherichia coli* and *Pseudomonas aeruginosa*. MgO nanoparticle concentrations ranging from 0.05 to 10.00 mg $mL^{-1}$ were investigated (Fig. 11). However, distinct inhibition-zone boundaries could not be identified reliably from the presented photographs. Consequently, the most and least sensitive strains and their inhibition-zone diameters cannot be established from this figure alone. The minimum inhibitory concentrations for *P. aeruginosa* and *E. coli* should be reported only from the corresponding broth-dilution measurements.

Differences in susceptibility may arise from variations in bacterial cell-wall composition and nanoparticle–membrane interactions. MgO nanoparticles can attach to cell surfaces, disturb membrane integrity, and promote leakage of intracellular constituents (Ganvir *et al.* 2026). Their antibacterial performance may additionally involve reactive oxygen species generation, local alkalinity, and $Mg^{2+}$ release. These combined effects can damage cellular proteins, lipids, and nucleic acids, eventually suppressing bacterial growth.

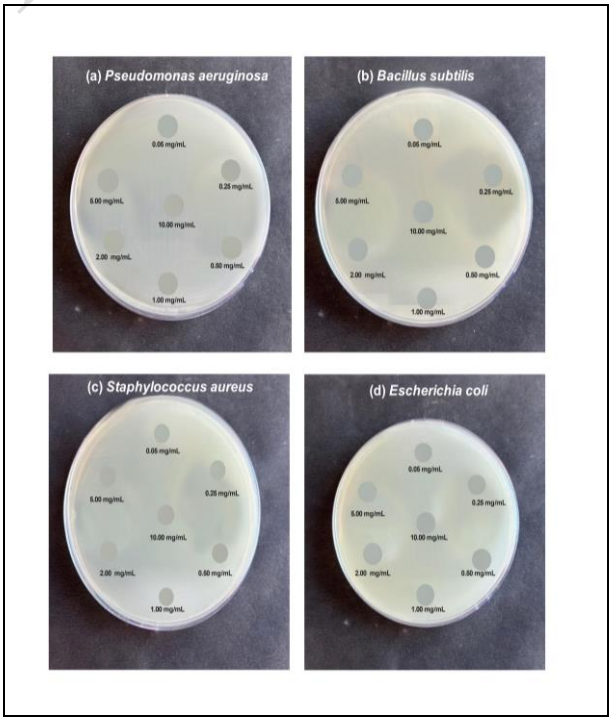


**Fig. 11: Antibacterial activity of green-synthesized MgO nanoparticles against (a) *Pseudomonas aeruginosa*, (b) *Bacillus subtilis*, (c) *Staphylococcus aureus* and (d) *Escherichia coli***

The antibacterial behaviour of magnesium oxide nanoparticles is primarily associated with reactive oxygen species generation, including hydroxyl radicals (•OH), superoxide radicals ($O_2^{\bullet-}$), and hydrogen peroxide ($H_2O_2$). The reactive species induce oxidative stress, weaken the bacterial cell envelope, raise membrane permeability, and promote leakage of intracellular components. They may also oxidize cellular proteins and damage genetic material, thereby limiting microbial growth. Direct attachment of MgO nanoparticles to the bacterial surface, $Mg^{2+}$ release, and the formation of a locally alkaline environment may further intensify membrane deterioration. Variations in inhibition-zone diameter among the tested strains can be linked to differences in cell-wall structure, surface characteristics, and resistance to oxidative stress. Although these combined processes explain the observed antibacterial response, the relative contribution of each pathway requires further investigation.

### 3.7 Catalytic Oxidation of Reactive Orange 16

The catalytic behavior of green-synthesized magnesium oxide nanoparticles was investigated using Reactive Orange 16 as the model contaminant. Two treatment systems, MgO/$H_2O_2$/hydroxylamine and MgO/NaClO/hydroxylamine, were evaluated and compared with corresponding controls lacking either MgO nanoparticles or hydroxylamine. Figure 12 shows the progressive reduction in the characteristic absorption band of Reactive Orange 16 at approximately 493 nm. Its decreasing intensity with reaction time indicated dye removal, while the nearly diminished band after 30 min demonstrated substantial decolorization.

The addition of hydroxylamine changed the removal efficiency from 67% to 89% in the MgO/$H_2O_2$ system and from 82% to 97% in the MgO/NaClO treatment. Control experiments containing only $H_2O_2$ or NaClO produced 28% and 42% removal, respectively. The improved response observed after introducing MgO nanoparticles confirmed their contribution to oxidant activation and dye–catalyst interactions. The MgO/NaClO/hydroxylamine combination exhibited the highest apparent degradation rate of 0.117 $min^{-1}$, compared with 0.074 $min^{-1}$ for MgO/$H_2O_2$/hydroxylamine. Similarly, iron oxide nanoparticles for methylene blue removal – Myristica fragrans-derived iron oxide nanoparticles achieved 85.59% MB removal within 180 min, with strong antioxidant activity ($IC_{50}$ = 40.88 µg $mL^{-1}$) and antibacterial performance (Salim *et al.* 2025). This difference may result from variations in reactive-species generation and oxidant stability. These systems should be described as MgO-assisted catalytic oxidation processes rather than Fenton-like reactions because MgO does not provide the iron redox cycle required for Fenton chemistry.

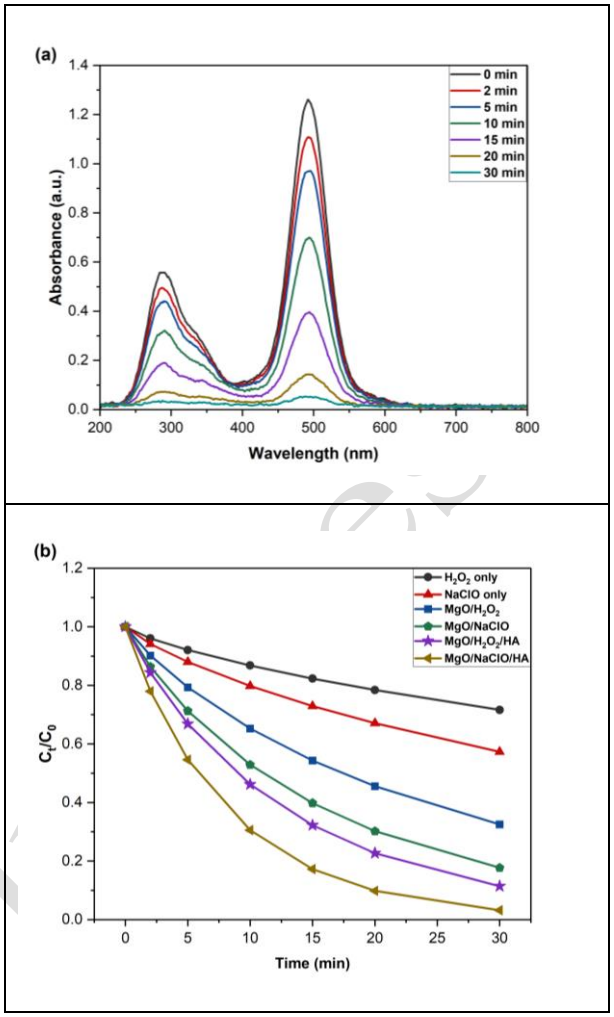


**Fig. 12: (a) Time-dependent UV–visible absorption spectra and (b) normalized concentration ratio (Ct/C0) of Reactive Orange 16 using MgO nanoparticles prepared with *Cardiospermum halicacabum* leaf extract**

**Table 8. Apparent rate constants for reactive orange 16 removal by different MgO-assisted oxidation systems**

| Process | MgO–$H_2O_2$ | MgO–NaClO | MgO–$H_2O_2$/HA | MgO–NaClO /HA |
|---|---|---|---|---|
| k($min^{-1}$) | 0.037 | 0.057 | 0.074 | 0.117 |

The rate constants previously reported for iron-based systems cannot be transferred to MgO because magnesium oxide does not undergo an $Fe^{3+}/Fe^{2+}$ redox cycle. Therefore, the four $k_{app}$ values must be calculated from the experimental Reactive Orange 16 data using:

$$\ln\left(\frac{C_0}{C_t}\right) = k_{app}t \qquad \ldots (10)$$

The MgO-assisted systems operate through surface adsorption, oxidant activation, and reactive-species formation rather than conventional Fenton

chemistry. Hydration and surface-peroxide development may be represented as (Mukherjee *et al.* 2025):

$$MgO + H_2O \rightleftharpoons Mg(OH)_2 \quad \ldots (11)$$

$$\equiv Mg - OH + H_2O_2 \rightleftharpoons Mg - OOH + H_2O \ldots (12)$$

For the hypochlorite treatment, the relative abundance of $OCl^-$and HOCl depends strongly on solution pH (Sharmiladevi *et al.* 2024):

$$OCl^- + H^+ \rightleftharpoons HOCl \quad \ldots (13)$$

Interactions between hydrogen peroxide and hypochlorite can also generate singlet oxygen. The resulting reactive oxygen species attack the azo chromophore and aromatic groups of Reactive Orange 16, producing smaller transformation products:

ROS + RO16 → degradation intermediates

Hydroxylamine may alter oxidant activation and reactive-species production; however, its enhancing effect must be confirmed from the measured rate constants. The system with the largest $k_{app}$ and removal percentage should therefore be identified as the most effective MgO-assisted catalytic oxidation treatment. It should not be described as a Fenton-like process because no iron catalyst is present.

## 4. CONCLUSIONS

Magnesium oxide nanoparticles were successfully synthesized through an environmentally responsible method using *Cardiospermum halicacabum* leaf extract. Taguchi L27 optimization and ANOVA demonstrated that extract concentration was the main factor governing nanoparticle yield, accounting for 54.02% of the observed variation. The optimized condition of 0.10 M $Mg(NO_3)_2{\cdot}6H_2O$, 100 g $L^{-1}$ leaf extract, 65 °C, and 75 min yielded 0.13913 ± 0.00035 g of MgO nanoparticles, closely agreeing with the predicted value of 0.13926 g. Among the predictive approaches, SVR showed superior accuracy with a cross-validated $R^2$ of 0.9999 and minimal residual error.

Spectroscopic and structural analyses verified the successful formation of crystalline cubic MgO, while the biological assays demonstrated concentration-dependent antibacterial effects. The nanoparticles also effectively promoted Reactive Orange 16 removal through oxidant-assisted catalytic oxidation. Hydroxylamine substantially enhanced the reaction, and the MgO/NaClO/hydroxylamine system delivered the best performance, with an apparent rate constant of 0.117 $min^{-1}$ and 96.8% removal within 30 min. Overall, the study establishes green-synthesized MgO nanoparticles as promising multifunctional materials for microbial control and treatment of dye-bearing wastewater. These results confirm that *Cardiospermum halicacabum*-mediated MgO nanoparticles are effective, low-cost multifunctional agents combining antibacterial action with rapid (30 min), high-efficiency (96.8%) dye degradation. Future investigations should examine catalyst recyclability, degradation-product toxicity, mineralization efficiency, reaction mechanisms, and performance in actual textile effluents.

## FUNDING

This research received no specific grant from any funding agency in the public, commercial, or not-for-profit sectors.

## CONFLICTS OF INTEREST

The authors declare that there is no conflict of interest.

## COPYRIGHT




## REFERENCES

Abdulhameed, A. S., Wu, R., Musa, S. A., Agha, H. M., ALOthman, Z. A., Jawad, A. H. and Algburi, S., Bisphenol-A-diglycidyl ether modified chitosan/nano-$SiO_2$ via hydrothermal process: A statistical modeling and adsorption mechanism for reactive orange 16 dye removal, *Int. J. Bio. Macromol.*, 256, 128267(2024). https://doi.org/10.1016/j.ijbiomac.2023.128267

Ahmad, A. R., Zaidi, S., Aslam, P. K. A., Arish, U. M., Khan, A. Y., Tariq, S. C. M. and Asiri, A. M., Removal of congo red from water by adsorption onto activated carbon derived from waste black cardamom peels and machine learning modeling, *Alexandria Eng. J.*, 71, 355–369(2023). https://doi.org/10.1016/j.aej.2023.03.055

Alanazi, A. A., Saber, W. I. A., AlDamen, M. A. and Elattar, K. M., Sustainable green synthesis of high-performance $Fe_2O_3$@$CeO_2$-pullulan nanocomposite for efficient dye removal, and antifungal applications, *Int. J. Bio. Macromol.*, 308, 142533(2025). https://doi.org/10.1016/j.ijbiomac.2025.142533

Amale, A. B., Satishkumar, P., Bhagat, P. R., Motghare, M. S. and Krishnaraj, C., Green Synthesis of ZnO Nanoparticles Using Azadirachta indica Leaf Extract for Rapid Catalytic Degradation of Organic Pollutants, *J. Environ. Nanotechnol.*, 15(2), 151–161

(2026). https://doi.org/10.13074/jent.2026.06.2612082

Badilli, B. N., Bulut Kocabas, B., Attar, A., Aktas, E. and Altikatoglu, Y. M. Sustainable synthesis of MgO nanoparticles from Persea americana for cultivar dependent nanostructure, environmental remediation and bioactivity supported by molecular docking, *Sci. Rep.*, 16(1), 13742(2026). https://doi.org/10.1038/s41598-026-44077-4

Boddu, S., Marri, B. P., Katika, R. M., Mikkili, I., Dulla, J., Allugunulla, V. N., Malladi, S. and Khan, A. A., Green Synthesis of Copper Oxide Nanoparticles (CuONPs) using Ricinus Communis: Efficient Photocatalytic Dye Degradation and Antibacterial Applications, *Water, Air Soil Pollut.*, 236(4), 209(2025). https://doi.org/10.1007/s11270-025-07841-2

Karthick, C., Shiny, H. B., Pandi, P. S. and Caroline, D. G., One-Pot Synthesized rGO–AgNP Nanocomposites for Sunlight-Assisted Removal of Coomassie Brilliant Blue: Kinetics, Isotherm and Antimicrobial Application, *Water, Air Soil Pollut.*, 237(17), 959(2026). https://doi.org/10.1007/s11270-026-09633-8

Chowdhury, L., Ebenezer, A. J. P., ShivaPrakash, S., Kirthiga, R., Mayakannan, S. and Subramaniam, M., Multi-objective optimization of heat-treated date palm seed biomaterials using genetic algorithms and Taguchi method, *Interact.*, 247(1), 179(2026). https://doi.org/10.1007/s10751-026-02515-9

Dhanaraj, K., Adhitiyan, T., Gubendhiran, S., Thenpandiyan, E., Ilaiyaraja, P., Sagadevan, S. and Suresh, G., *Cardiospermum halicacabum* leaf extract assisted Ag and Zn doped biocompatible nanohydroxyapatite photocatalyst for efficient dye degradation from wastewater, *Mater. Sci. Eng. B*, 308, 117568(2024). https://doi.org/10.1016/j.mseb.2024.117568

Dinesh, A., Kanmani Raja, K., Manikandan, A., Almessiere, M. A., Slimani, Y., Baykal, A., Saeed Alorfi, H., Hussein, M. A. and Khan, A., Sol-gel combustion synthesis and photocatalytic dye degradation studies of rare earth element Ce substituted Mn-Zn ferrite nanoparticles, *J. Mater. Res. Technol.*, 18, 5280–5289(2022). https://doi.org/10.1016/j.jmrt.2022.04.121

Dos Reis, G. S., Thivet, J., Laisné, E., Srivastava, V., Grimm, A., Lima, E. C., Bergna, D., Hu, T., Naushad, M. and Lassi, U., Synthesis of novel mesoporous selenium-doped biochar with high-performance sodium diclofenac and reactive orange 16 dye removals, *Chem. Eng. Sci.*, 281, 119129(2023). https://doi.org/10.1016/j.ces.2023.119129

Ganvir, H. V, Musrif, P. G., Satishkumar, P., Kadam, A. D., Saminathan, R. and Krishnaraj, C., Sustainable Synthesis of MgO Nanoparticles from Clerodendrum inerme Bast Fiber Extract: Physicochemical Characterization and Antibacterial Performance, *J. Environ. Nanotechnol.*, 15(2), 380–388 (2026). https://doi.org/10.13074/jent.2026.06.2622227

Guo, J., Yu, H., Wang, D. and Fan, L., Cavitation-enhanced carbonation for nano-ZnO synthesis via an ultrasonic–jet coupled reactor: Machine learning prediction and multi-objective optimization using a genetic algorithm, *Ultrasonics Sonochem.*, 129, 107859 (2026). https://doi.org/10.1016/j.ultsonch.2026.107859

Huang, J., Sun, J., Shao, K., Lin, Y., Liu, Z., Fu, Y. and Mu, L., Green Hydrothermal Synthesis and Applications of Sorbus pohuashanensis/ Aronia melanocarpa Extracts Functionalized-Au/Ag/AuAg Nanoparticles, *J. Renewable Mater.*, 11(4), 1807–1821 (2023). https://doi.org/10.32604/jrm.2023.023721

Hussain, N., Bilal, M., Afzal, M. Y., Shafaat, S., Amin, B. A. Z., Shah, F. and Shaikh, A. J., Eco-safe degradation of reactive orange 16 via adsorption-enhanced photocatalysis using $CoFe_2O_4$ nanoparticles, *RSC Adv.*, 16(23), 20658–20676 (2026). https://doi.org/10.1039/d6ra02108e

Kaur, A. and Pal, B., Photocatalytic activity of Ag@$TiO_2$ modified CoAl layered double hydroxide composite for the degradation of dye under visible and sunlight, *J. Water Process Eng.*, 82, 109500(2026). https://doi.org/10.1016/j.jwpe.2026.109500

Kavitha, K., Benitasherine, H. and Rajendran, S., *Cardiospermum halicacabum* leaves extract as a green corrosion inhibitor for mild steel in simulated oil well water medium, *Int. J. Corros. Scale Inhibition*, 10(4), 1646–1660 (2021). https://doi.org/10.17675/2305-6894-2021-10-4-17

Kiran, S., Albargi, H. B., Afzal, G., Aimun, U., Anjum, M. N., Qadir, M. B., Khaliq, Z., Jalalah, M., Irfan, M. and Abdullah, M. M., A zadirachta indica-assisted green synthesis of magnesium oxide nanoparticles for degradation of Reactive Red 195 dye: a sustainable environmental remedial approach, *Appl. Water Sci.*, 13(10), 193(2023). https://doi.org/10.1007/s13201-023-02000-6

Kotteeswaran, V., Ponsreeram, S., Mukherjee, A., Sadagopan, A. and Anbalagan, N. K., Green Synthesis of Silver Nanoparticles using Cardiospermum Halicacabum Leaf Extract and its Effect on Human Colon Carcinoma Cells, *Biomed. Pharmacol. J.*, 17(2), 949–963 (2024). https://doi.org/10.13005/bpj/2915

Lateef, S. A., Oyehan, I. A., Oyehan, T. A. and Saleh, T. A., Intelligent modeling of dye removal by aluminized activated carbon, *Environ. Sci. Pollut. Res.*, 29(39), 58950–58962 (2022). https://doi.org/10.1007/s11356-022-19906-4

Mohammad, S. I., Owida, H. A., Vasudevan, A., Arishi, A., Shaaban, S. M., Sammen, S. S. and Salem, A., Advanced antifouling performance of PSF HNT $Al_2O_3$ GO membranes through a synergistic approach using nanocomposite tuning and machine learning,

*Front. Environ. Sci.*, 13, 1644091(2025). https://doi.org/10.3389/fenvs.2025.1644091

Muhaymin, A., Mohamed, H. E. A., Hkiri, K., Safdar, A., Azizi, S. and Maaza, M., Green synthesis of magnesium oxide nanoparticles using Hyphaene thebaica extract and their photocatalytic activities, *Sci. Rep.*, 14(1), 20135(2024). https://doi.org/10.1038/s41598-024-71149-0

Mukherjee, S., Gupta, A. and Bhatnagar, T., Plant-Mediated Green Synthesis of α-$Fe_2O_3$ Nanoparticles from Chrysanthemum indicum Flower Extract: Applications in Photolytic Dextromethorphan Degradation, Dye Removal, and Antibacterial Activity Assessment, *Chem. Select*, 10(1), e202404574(2025). https://doi.org/10.1002/slct.202404574

Patel, B., Choudhary, N., Dudhagara, D., Shahid, M., Syed, R., Yadav, V. K., Sahoo, D. K. and Patel, A., Green synthesis of Ag-Fe bimetallic nanoparticles using fungal filtrates: unlocking multifunctional medical and environmental applications, *RSC Adv.*, 15(3), 1565–1575 (2025). https://doi.org/10.1039/d4ra07541b

Prajudtasri, N., Prachumrak, N., Phokha, S. and Utara, S., Green synthesis of $AgCu_2O$ nanocomposites via Melastoma saigonense extract: Physicochemical characterization and multifunctional bioenvironmental applications, *J. Sci. Adv. Mater. Devices*, 10(3), 100953 (2025). https://doi.org/10.1016/j.jsamd.2025.100953

Rao, D. P., Krishnasamy, V. D., Selvaraju, M., Sundramurthy, V. P., Kandavalli, S. R., Chitra, M. S., Sivasamy, N. and Thirumoorthy, P., Adsorptive removal of cadmium from electroplating wastewater using hybrid composite of thiol-grafted seed gum of Tamarindus indica and Teff hay biocarbon, *Zeitschrift Fur Physikalische Chemie*, 239(5), 633–654 (2025). https://doi.org/10.1515/zpch-2024-0715

Sadeghianmaryan, A., Zarbaf, D., Montazer, M. and MahmoudiRad, M., Green Synthesis of Organo-Montmorillonite/Silver Nanocomposites on Dyed Cotton with Vat Dyes to Achieve Biocompatible Antibacterial Properties on Fashionable Clothing, *J. Nat. Fib.*, 19(15), 10253–10268(2022). https://doi.org/10.1080/15440478.2021.1993494

Sadek, A. H., Fahmy, O. M., Nasr, M. and Mostafa, M. K., Predicting Cu(II) Adsorption from Aqueous Solutions onto Nano Zero-Valent Aluminum (nZVAl) by Machine Learning and Artificial Intelligence Techniques, *Sustainability (Switzerland)*, 15(3), 2081 (2023). https://doi.org/10.3390/su15032081

Sahith, V. N., Jagadeesan, A. K. and Sruthi, V. S., Sustainable Development of Magnesium Oxide Nanoparticles Using Pterocarpus santalinus and Their Antimicrobial Activity, *J. Environ. Nanotechnol.*, 14(2), 189–195 (2025). https://doi.org/10.13074/jent.2025.06.2521527

Salim, S., Hari, N., Sudhi, S. and Nair, A. J., Green synthesis, characterisation and bioactivity of iron oxide nanoparticles using Myristica fragrans leaf extract, *Microbe (Netherlands)*, 8, 100481(2025). https://doi.org/10.1016/j.microb.2025.100481

Sasi, S., Fathima Fasna, P. H., Bindu Sharmila, T. K., Julie Chandra, C. S., Antony, J. V, Raman, V., Nair, A. B. and Ramanathan, H. N., Green synthesis of ZnO nanoparticles with enhanced photocatalytic and antibacterial activity, *J. Alloys Compds*, 924, 166431 (2022). https://doi.org/10.1016/j.jallcom.2022.166431

Seghir, B. B., Hima, M., Moulatti, F., Sahraoui, I., Ben Amor, I., Zeghoud, S., Hemmami, H., Kouadri, I., Ben Amor, A., Messaoudi, M., Ahmed, S., Rebiai, A. and Pohl, P., Exploring the Antibacterial Potential of Green-Synthesized MgO and ZnO Nanoparticles from Two Plant Root Extracts, *Nanomater.*, 13(17), 2425(2023). https://doi.org/10.3390/nano13172425

Sharmiladevi, S., Ramesh, N., Prabhu, S. V and Mayakannan, S., Microwave-assisted functionalized biosorbent preparation using seed gum of Tamarindus indica: characterization and evaluation of Cr(VI) removal potency from tannery effluents, *Biomass Convers. Biorefine.*, 14(12), 13533–13545 (2024). https://doi.org/10.1007/s13399-024-05667-2

Vanitha, C., Abirami, R., Chandraleka, S., Kuppusamy, M. R. and Sridhar, T. M., Green synthesis of photocatalyst hydroxyapatite doped $TiO_2$/GO ternary nanocomposites for removal of methylene blue dye, *Mater. Today: Proce.*, 09203(2023). https://doi.org/10.1016/j.matpr.2023.02.354

Wu, R., Abdulhameed, A. S., Jawad, A. H., Musa, S. A., De Luna, Y., ALOthman, Z. A. and Algburi, S., An eco-friendly chitosan-genipin/$SiO_2$ composite for reactive orange 16 dye removal: Insights into adsorption statistical modeling and mechanism, *Int. J. Bio. Macromol.*, 270, 132329(2024a). https://doi.org/10.1016/j.ijbiomac.2024.132329

Wu, R., Abdulhameed, A. S., Selvasembian, R., Yousif, E., ALOthman, Z. A. and Jawad, A. H., Optimized Hydrothermal Synthesis of Chitosan-Epichlorohydrin/Nanosilica for Efficient Reactive Dye Removal: Mechanistic Insights, *Water, Air, Soil Pollut.*, 235(2), 128(2024b). https://doi.org/10.1007/s11270-024-06943-7